Journal of Applied Physics

RESEARCH ARTICLE | JUNE 24 2022

Turn all the lights off: Bright- and dark-field second-harmonic microscopy to select contrast mechanisms for ferroelectric domain walls

Peter A. Hegarty ; Henrik Beccard ; Lukas M. Eng ; Michael Rüsing

Check for updates

Journal of Applied Physics 131, 244102 (2022)
https://doi.org/10.1063/5.0094988

View Online Export Citation CrossMark

Articles You May Be Interested In

Green bands of the CsHg molecule

J. Chem. Phys. (May 1999)

Theoretical investigation of the CsHg molecule

AIP Conference Proceedings (January 1997)

Relativistic all-electron ab initio calculations of CsHg potential energy curves including spin-orbit effects

J. Chem. Phys. (December 1998)

Downloaded from http://pubs.aip.org/aip/jap/article-pdf/doi/10.1063/5.0094988/16509946/244102_1_online.pdf

AIP Advances

Why Publish With Us?

25 DAYS average time to 1st decision

740+ DOWNLOADS average per article

INCLUSIVE scope

Learn More

AIP Publishing

AIP Publishing

Journal of Applied Physics ARTICLE scitation.org/journal/jap

Turn all the lights off: Bright- and dark-field second-harmonic microscopy to select contrast mechanisms for ferroelectric domain walls

Cite as: J. Appl. Phys. **131**, 244102 (2022); doi: 10.1063/5.0094988
Submitted: 7 April 2022 · Accepted: 5 June 2022 ·
Published Online: 24 June 2022

View Online Export Citation CrossMark

Peter A. Hegarty,[1,a)] Henrik Beccard,[1] Lukas M. Eng,[1,2] and Michael Rüsing[1,a)]

AFFILIATIONS

[1]Institute of Applied Physics, TU Dresden, Nöthnitzer Strasse 61, 01187 Dresden, Germany
[2]ct.qmat: Dresden–Würzburg Cluster of Excellence—EXC 2147, TU Dresden, 01062 Dresden, Germany

[a)]**Authors to whom correspondence should be addressed:** peter_andrew.hegarty@tu-dresden.de and michael.ruesing@tu-dresden.de

ABSTRACT

Recent analyses by polarization resolved second-harmonic (SH) microscopy have demonstrated that ferroelectric (FE) domain walls (DWs) can possess non-Ising wall characteristics and topological nature. These analyses rely on locally analyzing the properties, directionality, and magnitude of the second-order nonlinear tensor. However, when inspecting FE DWs with SH microscopy, a manifold of different effects may contribute to the observed signal difference between domains and DWs, i.e., far-field interference, Čerenkov-type phase-matching (CSHG), and changes in the aforementioned local nonlinear optical properties. They all might be present at the same time and, therefore, require careful interpretation and separation. In this work, we demonstrate how the particularly strong Čerenkov-type contrast can selectively be blocked using dark- and bright-field SH microscopy. Based on this approach, we show that other contrast mechanisms emerge that were previously overlayed by CSHG but can now be readily selected through the appropriate experimental geometry. Using the methods presented, we show that the strength of the CSHG contrast compared to the other mechanisms is approximately 22 times higher. This work lays the foundation for the in-depth analysis of FE DW topologies by SH microscopy.

© 2022 Author(s). All article content, except where otherwise noted, is licensed under a Creative Commons Attribution (CC BY) license (http://creativecommons.org/licenses/by/4.0/). https://doi.org/10.1063/5.0094988

I. INTRODUCTION

Second-harmonic (SH) microscopy and polarimetry are powerful tools for the investigation of symmetry, phase transitions, and structure of crystalline materials, including novel topological materials, van-der-Waals, and other novel two-dimensional materials (2DMs), such as ferroelectric domain walls (DWs).[1–6] Recently, ferroelectric DWs have attracted considerable attention as they represent highly conductive quasi-2D sheets fully embedded within a non-conductive matrix; moreover, DWs can be rewritten, moved, or modified at will, for example, by applying electric fields. Despite these promising properties, the physical mechanisms of their electronic conductivity are not understood to depth. In this regard, SH microscopy allows for 3D profiling, real time imaging, and determination of the local symmetry properties within crystals.[2,7,8] In particular, recent SH polarimetry studies have revealed unusual symmetries and topological substructures of (conductive) DWs,[9,10] which are thought to be directly connected to the observed conductivity. Those polarimetry studies rely on the fact that changes in the local crystal structure and symmetry at the DW result in a modification of the local nonlinear optical (NLO) properties, i.e., the second-order nonlinear susceptibility, which in turn is detected via changes in the SH intensity or polarimetry signal. However, signal changes at DWs can also be caused by a manifold of other mechanisms, which carefully need to be taken into account for interpretation and separated if necessary.

SH contrast at ferroelectric DWs is generally explained in one of three mechanisms:

- (1) far-field interference of the SH signal from domains of different orientation rather than the DW itself;
- (2) Čerenkov-type phase-matching at the DW; and
- (3) the aforementioned changes in the local NLO properties at the DW.

Downloaded from http://pubs.aip.org/aip/jap/article-pdf/doi/10.1063/5.0094988/16509946/244102_1_online.pdf

© Author(s) 2022

In contrast, to the third mechanism, for the processes (1) and (2), no DW substructure generally needs to be assumed. In these models, the DW is considered to be a 2D boundary between ferroelectric domains of different orientation without any extension or substructure. This assumption is reasonable because based on theory and experiment, e.g., atomic resolution TEM, it is established that ferroelectric DWs are generally small on the order of just a few unit cells (<10 nm),[11–13] which is much smaller compared to diffraction limited focus spots (<500 nm). In (1) far-field interference, if the focus is placed at the position of a DW, SH light is generated in each of the neighboring domains as the focus spot covers both domains. If we assume, for example, two domains of opposite polarization direction, then the generated SH light between the two domains will be exactly out of phase due to the inverted sign of nonlinear susceptibility in domains of opposite orientation. In the far field, this SH light will interfere, which results in decreased observation of SH intensity from DWs.[6] As simulations and experiments show, when focus-induced polarization or other types of DWs, e.g., a-c domains, are considered, this model predicts also bright domain contrasts or even more complex DW signatures.[3,4,6]

The far-field interference contrast requires efficient SH generation from the surrounding domains. However, SH generation is forbidden for focused beams within the bulk of normal-dispersive materials.[14–16] Therefore, it is thought to be the dominating mechanism at the surface of bulk crystals, in thin films, or when the conditions for anormal dispersion are met.

In contrast, in (2) Čerenkov-type phase-matching, the DW functions as a source of defect wave vectors, assisting in the phase-matching in the SH process and hence leading to an increased signal generation from DWs. In contrast to far-field interference, mechanism (2) does not rely on SH generation from the surrounding bulk, but rather just the presence of the DW. Therefore, Čerenkov-type SH generation (CSHG) is thought to be the main mechanism for DWs within the bulk, allowing for large-scale 3D imaging of domain structures.[8,17–20] As is discussed in more detail below, this CSHG light is emitted at a discrete angle with respect to the incident light,[21,22] which is similar in geometry to the Čerenkov-light emitted from faster-than-light particles in matter. It was demonstrated that analyzing the angular distribution of the CSHG allows to gain in-depth insight into the local roughness of DWs well below the optical resolution limit; i.e., CSHG can also provide insight into local DW properties.[21,23]

During the process of a literature census on the topic of second-harmonic generation on ferroelectric domain walls, it was found that a large portion of the work is devoted to the CSHG mechanism[7,8,19–21,23–53] with at least 36 readily available publications. On the other hand, both phase interference[3,5,6,14–16,54–62] and changes in the non-linearity[2,9,10,63–70] have lower representation of 15 and 11 works, respectively, that we could find. As seen by the Venn-diagram of the census in Fig. 1, many works usually just consider a single mechanism within their interpretation, with only few works reporting on a combination of mechanisms.[4,71] This is usually of no concern, as the large majority of these works use SH microscopy as an imaging tool and analyze the large-scale distribution of domains and DWs rather than trying to infer a DW substructure. However, when not just qualitative but quantitative

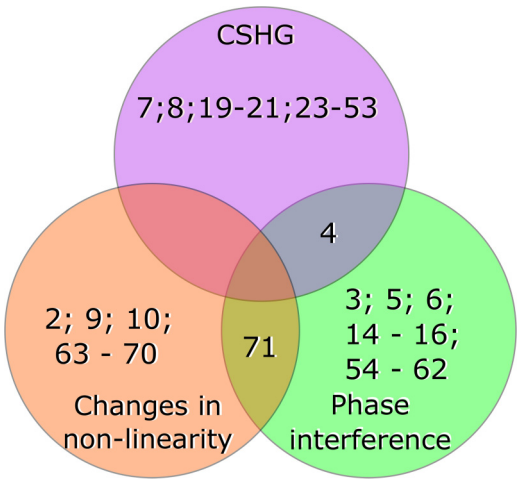

FIG. 1. Venn-diagram of the literature census performed prior to this work. References are grouped based on which mechanism they use to investigate in explaining the observed phenomena. We can see that the vast majority of works focus on a singular mechanism (with low amounts of overlap).

analysis of SH intensity is performed, for example, to unravel the substructure of DWs as in SH polarimetry[2,10] or to determine the sub-diffraction limit DW roughness through CSHG,[23] thorough consideration for the influence of each of the mechanisms needs to be given. Even when performing qualitative and especially for quantitative SH imaging, special care needs to be given when sudden contrast changes due to two competing mechanisms appear, which is possible close to interfaces. However, while CSHG is considered to be the main process behind imaging as shown in Fig. 1 and according to theory should always be present in any such measurement, there has been little effort to quantify or isolate CSHG in comparison with the other mechanisms. In this regard, efforts were made to quantitatively analyze both local changes to the non-linearity by Cherifi-Hertel *et al.*,[2,9,10] as well as phase-effects by Spychala *et al.*[3,4] by experiment, simulation, and modeling.

Hence, for the present work, we discuss and analyze possibilities to purposely either block or specifically select CSHG light. Based on this, we are able to provide an estimate of the strength of CSHG in comparison with the other mechanism(s), which can serve as a foundation for further efforts to quantitatively simulate CSHG, which so far has been illusive.

II. METHODOLOGY

A. Theory of Čerenkov SHG

During the SHG process, a measurable signal can only be obtained while the fundamental and frequency-doubled wave overlap in phase, allowing for a coherent buildup of SH radiation.[72] However, due to the difference in the respective refractive index for two given wavelengths, each wave will experience a different index and, therefore, an optical phase velocity. This results in a phase difference and wave-vector mismatch Δk between the fundamental

Downloaded from http://pubs.aip.org/aip/jap/article-pdf/doi/10.1063/5.0094988/16509948/244102_1_online.pdf

© Author(s) 2022

and second-harmonic wave vectors,[14,72] k_1 and k_2. For an ideal SHG process, the mismatch $\Delta k = 2k_1 - k_2$ is zero, which is only possible in a limited number of systems, such as birefringent crystals for specific fundamental wavelengths, e.g., congruent lithium niobate at a fundamental wavelength of approximately 1078 nm using the correct polarization.[14] In most general cases, there will always be a wave-vector mismatch as is depicted in Fig. 2(a) for a collinear SHG process.[7]

While it is difficult to obtain a perfectly matched process in a collinear geometry, the presence of DWs allows for highly efficient SHG as used in DW imaging.[7,8,17] As mentioned previously, DWs may serve as a source of (transversal) defect wave-vectors $\vec{G}$, which assist in the SHG process according to $2k_1 + G = k_2$ and, hence, can compensate for $\Delta k \neq 0$. The necessary defect wave-vectors are perpendicular to the DWs and the incident fundamental wave as shown in Fig. 2(a). The result is a non-collinear emission of SHG signal at a specific angle α with respect to the optical axis, thereby leading to a solely *longitudinal* phase-match $2k_1 - k_2\cos(\alpha) = 0$.

Similar to its particle physics counterpart, the direction into which CSHG light is emitted within a medium depends on the ratio between the speed of light at both the fundamental and second-harmonic wavelength and, therefore, the respective refractive indices according to Refs. 21 and 73,

$$\cos(\alpha) = \frac{n_1}{n_2}. \tag{1}$$

Kämpfe *et al.* have previously shown the existence of collinear CSHG at inclined DWs in lithium niobate[7] as well, which potentially provides additional insight into the DW substructure. However, as mentioned in Sec. I, in this work, we will assume the DW to be a 2D boundary between domains and as such will focus only on non-collinear CSHG, and therefore, we will not consider any additional substructure of the DW.

The angle α calculated via Eq. (1) is only valid while within the sample itself. In order for the CSHG light to be detected, it must leave the sample and is refracted at the sample interface. In our experiment, we will consider a sample–air interface. As the refractive index of the crystal is considerably larger than that of air, the experimentally observed emission angles will, therefore, be larger than the original emission angle within the crystal. This oblique emission can enable separation of CSHG from signal contributions resulting from the aforementioned other two mechanisms, (1) far-field interference and (3) local changes to the nonlinearity, which are predominantly emitted in a collinear manner (a comparison of emission characteristics is presented in Sec. S2 of the supplementary material).

Based on the difference in the emission direction, we propose two methods with which to block or isolate CSHG light:

- The first utilizes the collection properties of a microscope objective lens in a forward direction. The numerical aperture (NA) for a lens defines the upper limit α_u for angles that an objective lens is capable of either emitting or, more importantly, collecting via $NA = n \cdot \sin(\alpha_u) \Rightarrow \alpha_u = \arcsin(NA/n)$ with the refractive index n of the collection environment, usually air ($n = 1$). Light traveling at an angle below α_u then is collected, while that emitted at a larger angle than α_u cannot. Inversely, for light emitted from the crystal at a given emission angle α_e, there is a minimum collection NA required to collect the signal. Through variation of the collection NA, it should, therefore, be possible to block the collection of CSHG light with a sufficiently small NA. A principal sketch is shown in Fig. 2(b).
- The second method involves the use of apertures upon the crystal surface that are deposited in this work by evaporation

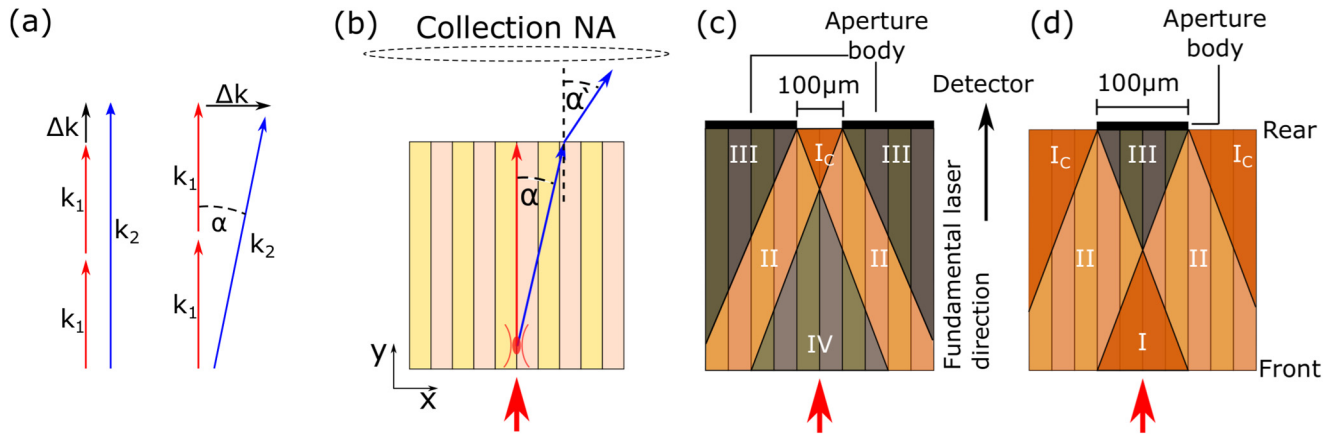

FIG. 2. (a) Vector diagrams depicting both collinear and non-collinear phase-matching during SHG. (b) Principal sketch of the collection of an SHG signal from within a ferroelectric crystal and a visualization of the influence of the collection NA with the incoming laser direction indicated by the red arrow. (c) Sketches of the expected CSHG signal pattern when using bright-field (c) or dark-field (d) apertures. Color indicates the collection of the CSHG signal, while opacity represents the respective signal strength. Note that the sketches only consider CSHG light. As a result of the aperture blocking, we observe a number of different region types: (I) full CSHG collection, (I_C) full CSHG collection and collection of collinear signal; (II) limited CSHG collection; (III) no signal collection; and (IV) only collinear signal collection.

Downloaded from http://pubs.aip.org/aip/jap/article-pdf/doi/10.1063/5.0094988/16509946/244102_1_online.pdf

© Author(s) 2022

with the help of shadow masks. The apertures consist of either two regions separated by a well-defined gap, allowing for bright-field SH microscopy, or a single broader region, granting access to dark-field SH microscopy. The use of such apertures on the crystal surface allow for targeted selection of signal contributions by blocking light of a certain emission direction and point of emission. The situation for the bright-field aperture is depicted in Fig. 2(c). Here, collinear SHG light emitted directly beneath the gap will be able to exit the said gap, while obliquely emitted CSHG light will experience a lateral displacement while propagating through the crystal and hence be blocked by the aperture body. Inversely, for a dark-field aperture as shown in Fig. 2(d), collinear light will be blocked by the aperture, while CSHG light can pass by the aperture and be collected by the microscope objective lens. Employing each type of aperture, therefore, leads to the emergence of a number of regions within the crystal from which CSHG is either collected or blocked. Example regions are indicated in Figs. 2(c) and 2(d) in color scale for bright-field and dark-field SH microscopy, respectively.

For bright-field SH microscopy [Fig. 2(c)], we obtain a total of four discernible regions with respect to CSHG. The first of these regions, region IV, is a central triangle with the front crystal surface as its base from which no CSHG light is collected, as any CSHG beams experience a sufficiently large lateral displacement to arrive at the rear surface directly beneath the aperture body. A second triangular region (I) emerges at the rear surface within the gap of the aperture from which the full collinear and non-collinear signal is collected. The third region (II) is a split pattern bordering on the first triangular region. Here, only half of the CSHG light is collected, namely, that which is emitted toward the aperture gap, forming two stripes on either side of the central triangle. Finally, we observe a second split region (region III) beneath the aperture body consisting of two right-angled triangles bordering on the previous stripes. Within this region, both CSHG light and collinear signal are blocked by the aperture. It is important to note that the angle α between both the sides of region IV, as well as region II, and the optical axis is equal to the CSHG emission angle at a given wavelength.

In contrast, dark-field SH microscopy [Fig. 2(d)] will show a complementary pattern to the bright-field variant. Once again, we see two triangles beneath the aperture. CSHG light emitted from the triangle based on the front surface (region of type I) is now fully collected, while the "rear" triangle is entirely blocked by the aperture body (type III region). In the dark-field image, we can further differentiate between two sub-types of type I regions, namely, the pure type I region, from which *only* CSHG is detected, and a type-I_C region, from which both CSHG and collinear signal are collected. Furthermore, we obtain similar stripe-shaped regions of type II from which only half of the CSHG light is collected, which results in a lower collected signal compared to the surrounding type I region.

For each type of aperture, the central triangle (I and IV, respectively) beginning at the front surface is the main region of interest as it is here that either the CSHG (bright-field) or collinear (dark-field) signal is fully blocked by the aperture within said regions. In the case of bright-field SH microscopy, it is then possible to analyze only the contributions based on mechanisms (1) and (2), most importantly at the crystal surface. Similarly, dark-field SH microscopy allows for analysis of only CSHG contributions to the signal generated within the crystal, allowing for a more quantitative analysis.

B. Experiment

The investigated samples are z-cut periodically poled lithium niobate (PPLN) with a 31 μm periodicity that were cut into $3 \times 1 \times 1\,\text{mm}^3$ (x, y, and z dimensions, respectively) pieces and then illuminated upon their y-face. Recent works concerning the analysis of lithium niobate using second-harmonic microscopy have primarily utilized the z-cut geometry,[8,21,23] whereas in this work, we investigate the y-cut geometry to offer a comparison. In order to observe the effect of an aperture upon the rear surface of the sample, we evaporated two types of apertures onto the surface of the samples using physical vapor deposition (PVD) via thermal evaporation. The apertures consist of an initial chromium layer with a thickness of 15 nm followed by a thicker gold layer of 135 nm to obtain a desirably low transmission through the aperture body. The respective aperture type was created with the help of shadow masks to obtain the desired 100 μm size of the aperture bodies and gap in the case of the bright-field aperture.

The samples were then examined using a commercial laser scanning microscope (Zeiss LSM980MP), which uses a tunable Ti: Sa laser source (Spectra Physics InSight X3, 690–1300 nm, 3,5 W, <120 fs pulse width). Each measurement was recorded in a transmissive geometry using a focusing numerical aperture of NA = 0.8. For the first method outlined above, the collection numerical aperture was varied between NA = 0.10 and NA = 0.55 to study the effect on the gathered signal. For the second isolation method using apertures, the collection NA was kept constant at NA = 0.55. The fundamental pump beam was linearly polarized parallel to the crystallographic x axis, while the collected SH light was unpolarized, i.e., contained light of all polarization directions.

III. RESULTS AND DISCUSSION

A. Variation of NA

The influence of the collection NA was investigated by recording scans in an xy-plane through the crystal with the laser incident from the y-direction, while varying the value of the collection NA. From this depth-resolved scan, the lateral profile was extracted (1) at the surface and (2) 50 μm below the surface, representative of the bulk medium (see Sec. S1 in the supplementary material). The signal originating within the domain region in the surface profiles was averaged to obtain the surface SHG signal, while a number of DWs within each profile in (2) were averaged to obtain the normalized DW signal without the influence of surface SHG. Due to our setup limiting the collection NA to 0.55 as an upper limit, the signal values obtained were then normalized to the signal collected with an NA of 0.55, resulting in values between 0 and 1. This is presented as a scatterplot in Fig. 3(a) for a fundamental wavelength of 900 nm.

SHG in a bulk medium is the result of dipole emissions within the medium itself, with said dipoles exhibiting an emission

Downloaded from http://pubs.aip.org/aip/jap/article-pdf/doi/10.1063/5.0094988/16509948/244102_1_online.pdf

© Author(s) 2022

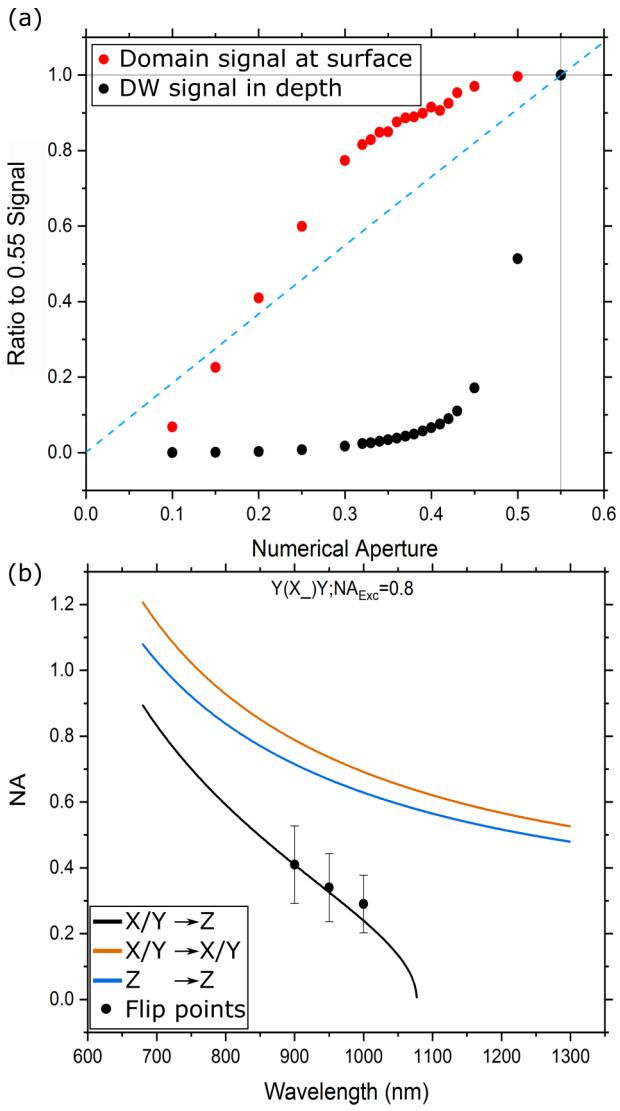

FIG. 3. Subfigure (a) shows the collected SH signal from both the sample surface and the domain walls within the bulk dependent on the utilized collection NA for a focusing NA of 0.8 and a fundamental wavelength of 900 nm. We see two distinctly different behaviors indicative of multiple mechanisms. Subfigure (b) shows the comparison of the determined threshold NAs for the sharp increase in DW signal compared to the theoretically expected thresholds.

pattern proportional to $1 - \cos^2(\alpha)$, where α is the angle between the direction of the dipole and the observed direction in space. This implies that the maximum signal contribution is at a 90° angle to the dipole orientation. The largest contributions to the total signal would be expected closely around the axis perpendicular to the dipole orientation. In the present experiment, the x-polarized fundamental beam was incident parallel to the lithium niobate y axis. Based on the non-linear optical tensor of lithium niobate, the largest contribution to the generated non-linear polarization is aligned parallel to the z axis,[5] and the maximum of the dipole emission will, therefore, be parallel to the y axis and, hence, along the forward direction (see Sec. S2 in the supplementary material). Our collecting objective lens is located along the y axis facing the crystal, i.e., in the direction of maximum emission. The generated SH light should, therefore, be detectable with any NA larger than zero, with an initial steep increase in the signal, which flattens out as the collecting NA is increased. We would assume the SHG stemming from the domains at the crystal surface to exhibit a similar behavior, as they are expected to follow "traditional" SHG, whereas we expect a different, if currently unknown, behavior for the domain walls. The dashed line included in the figure represents the theoretical behavior for an emitting dipole within the crystal as one would expect from SHG (see Sec. S2 in the supplementary material).

We see that for the available collection NA range, the surface signal behaves roughly like one would expect from a dipole emission that occurs shortly below the sample surface. That is, an initial linear increase in the signal with an increase in collection NA slowly evens out toward our upper NA limit of 0.55. This agrees well with the expectation that the observable SHG signal from the domains at the surface is caused by the excitation of local dipoles within the medium and is emitted in the characteristic $1 - \cos^2(\alpha)$ pattern.

On the other hand, the signal emitted from the DWs shows drastically different behavior with respect to the NA variation. The initial linear slope for lower NAs below approximately 0.3 NA is noticeably flatter, which transitions into a sharp increase in the signal after a certain threshold NA around 0.4. This increase above a certain threshold is best explained by the sudden collection of the CSHG emission by the collection NA when reaching the threshold NA. This indicates that the variation of the collection NA represents a valid possibility to filter out the CSHG signal contributions stemming from ferroelectric domain walls (see Sec. S3 in the supplementary material).

In order to verify the assumption that the additional signal is indeed CSHG, the theoretical minimum collection NA required to collect the CSHG emission at a given wavelength was calculated and plotted in Fig. 3(b) as the solid lines for three possible polarization combinations of incoming and detected waves. This is done by calculating the CSHG emission angle α_e based on the refractive indices provided by Jundt and compiled in *Properties of Lithium Niobate* by Wong[73] and subsequently the propagation angle α_p in air after refraction out of the crystal, which translates to the minimum collection NA as $NA_{min} = arcsin(\alpha_p)$.

Additionally, we calculated the discrete derivative of the signal plotted in Fig. 3(a) and identified the collection NA at which the change in the discrete derivative was the largest as the threshold NA for each data set recorded with a number of measured wavelengths (900, 950, 1000 nm). These measured thresholds were added as scatter points to Fig. 3(b). As seen from that figure, the determined thresholds coincide within the confidence interval with the theorized minimum required numerical aperture for collection of a process involving a fundamental wave polarized parallel to the crystallographic x- or y axis and a second-harmonic wave polarized parallel to the z axis. Hence, it stands to reason that the signal contribution that results in the sharp increase in Fig. 3(a) is, in fact,

Downloaded from http://pubs.aip.org/aip/jap/article-pdf/doi/10.1063/5.0094988/16509946/244102_1_online.pdf

© Author(s) 2022

caused by CSHG of the proposed model. We can, therefore, confirm that a variation of collection NA can be elegantly used as a method to block said CSHG.

As theory and experiment agree for the process generating a z-polarized SH from an x-polarized fundamental beam, we would expect the theoretical calculations for other combinations of polarizations to coincide with reality equally well. This, however, means that due to our upper limit of 0.55 NA for the available collection NAs, our system will have difficulties in analyzing the other two possible processes, i.e., either the generation of an x-polarized SH beam from an x-polarized fundamental or the generation of a z-polarized SH beam from a z-polarized fundamental. Due to our comparatively low NA limit, we would be unable to detect the change in the collected signal, as the threshold lies above our available NA. The analysis would have to be performed at a much higher fundamental wavelength range above 1140 nm; however, this wavelength range shows little change in the required collection NA with an increase in fundamental wavelength, making differentiation of the behavior at specific wavelengths more difficult. We would, therefore, also expect the results of the experiments involving the use of apertures to coincide with the (x/y → z) curve and will only perform the measurements with an x-polarized fundamental beam with the available system, where our upper limit of $NA = 0.55$ still permits detection.

B. Inclusion of surface apertures

In addition to the previously fabricated samples with their respective aperture type, a reference image was recorded with a third crystal from the same wafer for each wavelength. The two-dimensional depth scan images are shown in Fig. 4 as a 3 × 3 grid in which the wavelength increases from left to right from 850 to 950 nm in 50 nm steps. Each image shows the front-to-back scan starting at the bottom of the respective image, with the respective aperture located at the top of the image. It is important to note that each aperture type is a different crystal and, therefore, will show slightly different domain walls due to slight kinks in the DWs as a result of the poling process.

The images recorded with a fundamental wavelength of 850 nm [Figs. 4(a), 4(d), and 4(g) for reference, bright-field, and dark-field, respectively] readily show the changes in the signal that each type of aperture causes. The reference image in Fig. 4(a) displays both the surface SHG (broader bright horizontal strip along the bottom of the image) and the CSHG from the DWs (vertical lines) across the entire image width and shows no discernible influence of the fundamental wavelength.

As predicted in Fig. 2(c), the presence of a bright-field aperture on the rear surface of the crystal results in the CSHG emission being blocked from a triangular central region as well as two further areas directly beneath the aperture body in Figs. 4(d)–4(f), comparable to regions III and IV in Fig. 2(c). The CSHG signal from DWs that was previously visible across the entire image can now only be seen in two broader streaks of the type II region that overlap directly beneath the aperture opening at the rear surface. Additionally, we can observe that the DW signal within this overlapping region is stronger than within each separate streak, as the two CSHG beams emitted either side of the DW are each collected. Comparison of the signal collected from the type II and type I regions shows that the signal of the latter is approximately twice as strong as the former and, therefore, a simple linear superposition. Finally, the surface SHG recorded directly below the aperture at the bottom of the image contains only the non-CSHG contributions as is visible by the dark vertical lines in place of the bright DWs one can observe in the reference image.

Similar to the bright-field aperture image, the dark-field images [Figs. 4(g)–4(i)] reproduce the expected pattern shown in Fig. 2(d). The fully blocked region consists of a smaller triangular region (type III) directly below the aperture body. Full CSHG, but no collinear signal, is collected from a larger triangle below the blocked area with its base on the front surface (type I region) as well as from either side of the aperture. Similar to the bright-field case, only half of the CSHG is collected in two diagonal streaks that overlap directly beneath the aperture [type II regions in Fig. 2(d)], as one of the CSHG beams is blocked by the dark-field aperture. Contrary to the prior images, however, this now means that these streaks appear darker than the surrounding regions from which the full CSHG signal is collected. Finally, the surface directly below the aperture body, thus the lower edge of the central type I region, does not appear to emit any signal. Based on a comparison of Figs. 4(d) and 4(g), we can already qualitatively show that the use of on-surface apertures presents a potent method for separating SH signal contributions from DWs based on the absence of the respective signal contribution at the surface of the sample.

As is visible in Fig. 3(b), the minimum collection NA required for detection (and, therefore, also the original emission angle within the crystal with respect to the optical axis) decreases with higher wavelengths. Based on this, we expect this behavior to be reproduced in the images recorded with each kind of aperture. Within each row of Fig. 4, the same aperture type is used and instead the fundamental wavelength is varied. For the bright-field images, the lower emission angle results in the central blocked type IV region decreasing in size for a larger wavelength. At the same time, it is possible to observe that the shape of the region becomes more acute, i.e., the angle between the sides of the region and the vertical axis is smaller due to the lower CSHG emission angle. Both effects can be observed within Figs. 4(d) through 4(f). Similarly, the type II region of single CSHG collection shows a slightly smaller angle with regard to the vertical axis in Fig. 4(f) compared to Fig. 4(d), which is to be expected as the said angle should be equal to the CSHG emission angle α_e within the crystal. In the dark-field images, the entirely blocked type III region increases in size with an increasing fundamental wavelength, which is expected due to the progressively lower emission angle at larger wavelengths.

The aforementioned change in angle can readily be explained by the wavelength dependence of the CSHG emission angle. In order to verify that the changes in Fig. 4 are in fact caused by CSHG, the angle between the sides of the triangle and the vertical axis was calculated, as this angle should be equal to the CSHG emission angle. This was done by choosing a series of signal thresholds, which were applied to the image as a filter, i.e., pixels with a higher or lower signal appear white or black, respectively. This generated a sharper contrast between the region generating the signal and the region without the signal (see Sec. S5 in the

Downloaded from http://pubs.aip.org/aip/jap/article-pdf/doi/10.1063/5.0094988/16509946/244102_1_online.pdf

© Author(s) 2022

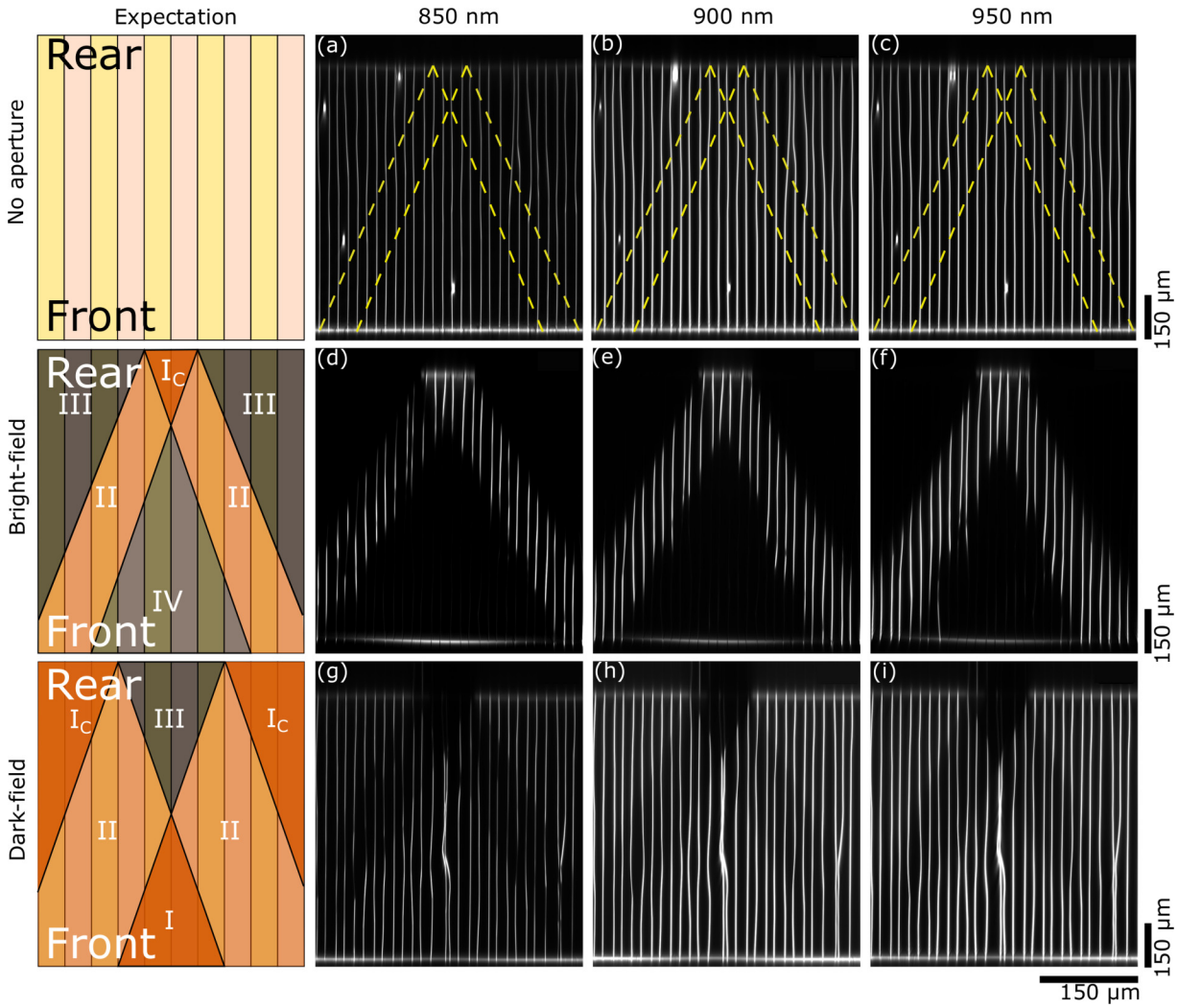

FIG. 4. Two-dimensional SHG scans of lithium niobate crystals using no aperture [(a)–(c)], bright-field aperture [(d)–(f)], and dark-field aperture [(g)–(i)], recorded for a 850, 900, and 950 nm fundamental wavelength. The external scale bars represent the actual dimensions within the crystal. We see the emergence of the expected patterns based on Fig. 2(c) for each aperture type. As mentioned in Sec. II, each type of aperture was created upon a different crystal.

supplementary material). This sharper contrast allowed for a more precise determination of the border between the visible domain walls and the dark region above them. The top end of each domain wall within each binary image was located with the image manipulation software ImageJ and translated into the actual position within the sample crystal. These positions were then used to perform separate linear fits of the left and right side of the enclosed triangle using the standard form of $y = Ax + B$. The average slope was calculated for each wavelength, averaging over the series of signal thresholds. The average slope A correlates with the angle between the region flank and the vertical axis α as $\alpha = \arctan(1/A)$.

The resulting slope angles for both the left and right flank of the triangle are plotted for each wavelength alongside the theoretical CSHG emission angle in Fig. 5. Based on the calculated threshold collection NAs shown in Fig. 3, we would expect the calculated angles to follow the expected behavior for the (x/y → z)-process. As is visible in Fig. 5, this holds true for the investigated wavelengths, as both the general wavelength dependence, i.e., a decrease in the emission angle with increasing fundamental wavelength, as well as the actual angles best agree with the curve representing the (x/y → z)-process. It is interesting to note that the angles of the right flank are slightly lower than those of the left flank; however, this effect is not particularly pronounced and is assumed to be caused by the non-ideality of the investigated DWs; i.e., slight kinks or meanderings of the respective DWs result in a less obvious border to the dark region.

Downloaded from http://pubs.aip.org/aip/jap/article-pdf/doi/10.1063/5.0094988/16509946/244102_1_online.pdf

© Author(s) 2022

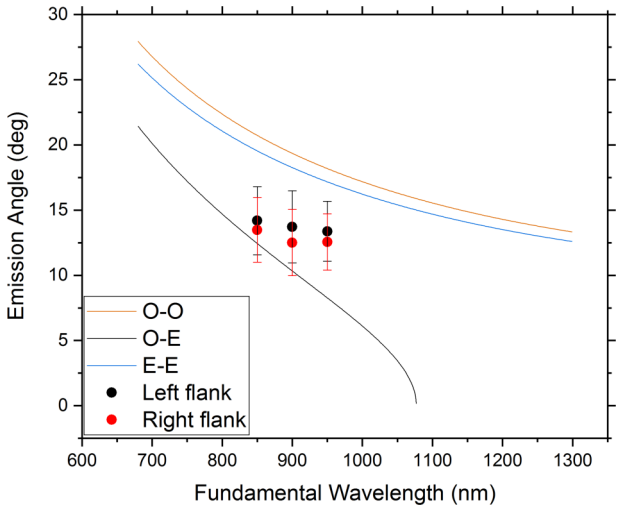

FIG. 5. Inclination angles of the region from which the CSHG signal is blocked, calculated from the average slope A of the triangular region in Figs. 4(d)–4(f) as $\alpha = \arctan(1/A)$. It is possible to compare Fig. 5 to Fig. 3(b) as the measured threshold NA is related to the emission angle α via $NA = n_{LN} \sin\alpha$; i.e., the axis of Fig. 3(b) is a rescaled counterpart of the axis shown in Fig. 5. In comparison with Fig. 3(b), the emission angles calculated from the average slope are slightly further from the theoretically expected curve.

In addition, the periodicity of 31.7 μm, i.e., a DW every 15.85 μm, results in a lower number of visible DWs, which makes the determination of the correct slope through all DWs in the image more difficult. As a result, the margin of error is relatively large compared to the determined angle at approximately 30% of the calculated angles due to the fact that the angles to be calculated are only around 10°–15°. While this may hinder the exact determination of the CSHG emission angle, the behavior is still best explained by CSHG of a z-polarized SH beam from an x-polarized fundamental wave.

C. Strength of CSHG

On-surface apertures not only allow us to qualitatively separate the signal contributions stemming from different SHG mechanisms, but also to make initial quantitative statements concerning the comparative strength of CSHG. This can be done by analyzing and comparing the SH signal generated at the front surface of the crystal for the case of the bright-field aperture with that of the reference crystal. This was done by extracting the horizontal line-profile across the image at the position of the crystal surface. Each profile was then normalized to the respective signal level of the domain region, i.e., the surface signal of the crystal itself. Figure 6 shows the extraction location from within the bright-field image along with the respective line-profile at the surface. In the reference scans, the DW signatures consist of positive peaks compared to the surrounding domain, whereas the DW signatures are local minima if CSHG emission is blocked [compare Figs. 4(a) and 4(d)]. This results in two distinct profiles as shown in Fig. 6(b), where the

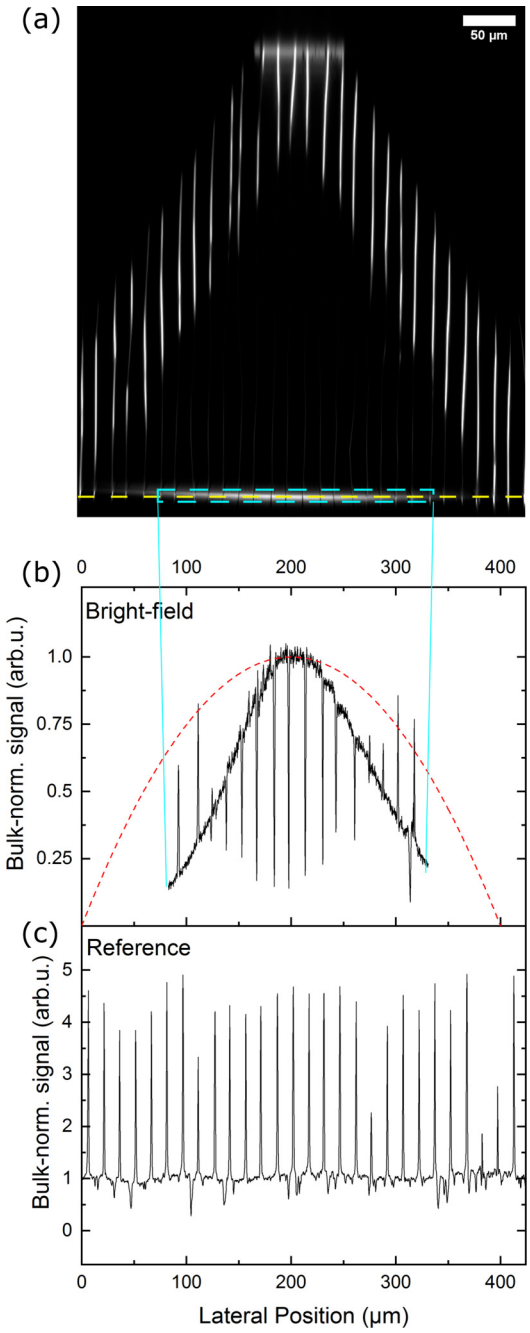

FIG. 6. Subfigure (a) shows the region and lines from which the signal profiles were extracted in order to calculate the comparative strength of CSHG for the case of the bright-field image recorded at 900 nm. Subfigure (b) depicts the normalized profiles for both the bright-field and reference image at 900 nm. The red-dashed line represents the qualitative profile calculated for a dipole emitter placed at the front surface and verifies that the parabolic shape of the actual profile is not caused by the loss of CSHG signal contributions. Subfigure (c) shows the normalized signal profile across the reference crystal at a fundamental wavelength of 900 nm.

Downloaded from http://pubs.aip.org/aip/jap/article-pdf/doi/10.1063/5.0094988/16509946/244102_1_online.pdf

© Author(s) 2022

profiles for both a bright-field aperture and a reference scan are depicted on the top and bottom, respectively. In order to verify that the observed profile envelope was not a result of the blocked CSHG, we qualitatively simulated the expected profile with an identically sized sample assuming a surface with no DWs but similarly with a bright-field aperture on the rear surface. The curve representing this theoretical profile is underlaid in Fig. 6(b) for the bright-field curve.

The theoretical calculations reproduce a similar parabolic envelope as observed in the experimental data, in that we observe a maximum at the center of the aperture gap and a decrease in the gathered signal toward either side. The sharper decline of the experimental signal is thought to be most likely caused by dissipative effects within the sample itself, which were not considered in the simplified calculation (see Sec. S6 in the supplementary material). Additionally, the calculation simply assumes a point-shaped dipole placed at the front surface from which the amount of the collected signal is determined. However, due to the diffraction limited size of the focus spot, a larger region of the crystal will generate an SH signal, and consideration thereof would result in a narrower parabola, closer to the measured profile.

Recent simulations by Rüsing *et al.*[6] have shown that the signature of a DW illuminated by an x-polarized beam incident along the crystal y axis, as investigated in this work, should indeed be a local minima with a relative value of approximately 60% of the surrounding domain signal. The bright-field measurement that excludes any CSHG emission shows a ratio between the DW signature and the surrounding domain signal of 0.23, slightly below the contrast between DW and the domain simulated from the signal stemming from phase interference and local changes to the non-linearity. The performed simulations were at the time focused on the backward-emitted signal stemming from the DWs. In general, however, forward-emitted SHG is noticeably stronger due to, among other effects, a considerably higher coherent interaction length of the SHG process (compare Amber *et al.*[5]). As such, it seems reasonable that the contrast ratio between the surface signal and the DW signature is lower in the forward-emitted case. In comparison, the ratio between the DW signature and the domain signal in the reference scan, i.e., with all mechanisms participating, is considerably higher at approximately 4.5. The CSHG contributions must overcome the destructive interference of the collinear signal, i.e., must compensate for the difference between the DW signature and the domain signal of 0.77. We would, therefore, assume that the pure CSHG signal would possess a normalized value of 5.27, which is approximately 22 times stronger than the DW signature in the collinear case.

Additionally, the normalized profiles are plotted in Fig. 7 for a variation of the collection NA. As with the use of the aperture, we observe a switch from a positive to negative DW signature at the surface for sufficiently low collection NAs and, therefore, the same behavior as when using on-surface apertures. The amplitude of the DW signatures for both edge cases is also similar to those of the aperture images, i.e., approximately 3.2 for the maximum NA of 0.55 and 0.2 for the lower limit of 0.10 NA. This serves as a further indicator that both experimental methods applied in this work can be used to isolate SHG signal contributions for future separate analysis.

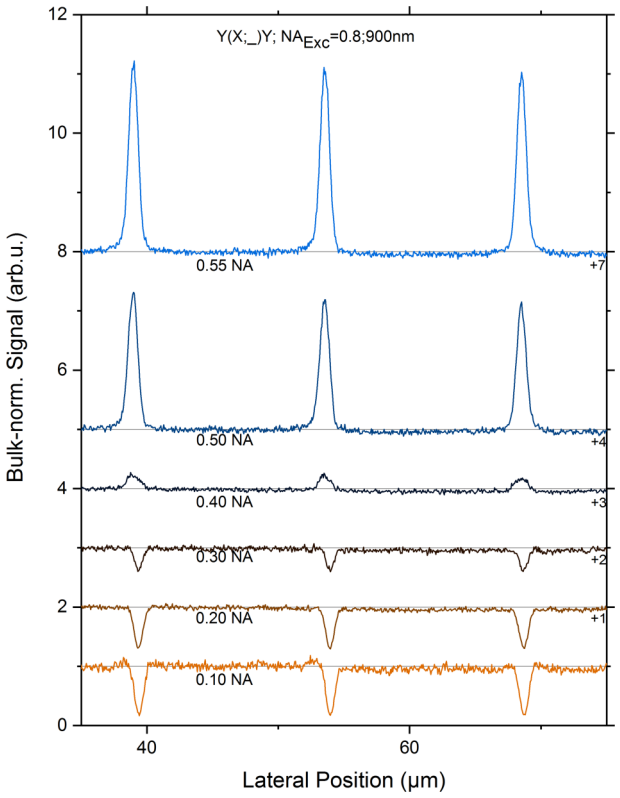

FIG. 7. Line profiles extracted at the surface of the reference sample while varying the collection NA. Similar to the use of apertures, we can observe the change from the positive DW signature at higher NA to the negative signature of the same magnitude of 0.2 for lower NA, i.e., the collection of the purely collinear signal.

IV. CONCLUSION

In this work, we have investigated methods with which it is possible to separate signal contributions in second-harmonic microscopy. It was shown that obliquely emitted CSHG light can be blocked from the detector path by decreasing the numerical aperture of the collection objective lens. Furthermore, the use of on-surface apertures can be used to either isolate CSHG or block it, which allows studying the effects of phase interference and changes in the local non-linearity of DWs under SH microscopy. Finally, we have gained an initial estimate on the comparative strength of CSHG compared to both other mechanisms as well as showing that all three effects occur simultaneously and, therefore, require differentiation during quantitative analysis.

While SH microscopy is without a doubt a potent and flexible tool for the investigation into novel systems, more work is required to separate and fully understand the underlying physical behavior (s). Analogously to Cherifi-Hertel *et al.*[10] and Spychala *et al.*,[3] the mechanism of CSHG requires future detailed analysis, investigation, and quantitative modeling. The inclusion of polarimetry could allow for an additional parameter with which to select

Downloaded from http://pubs.aip.org/aip/jap/article-pdf/doi/10.1063/5.0094988/16509946/244102_1_online.pdf

© Author(s) 2022

certain signal contributions, thereby allowing for a more selective investigation of material properties under SH microscopy.

Ideally, this first investigation into the isolation and properties of CSHG can form the basis of a more detailed understanding of SH microscopy on ferroelectric domain walls.

SUPPLEMENTARY MATERIAL

See the supplementary material for additional information on the data extraction procedures, emission behavior analysis, calculation of the emission angles, and expected surface profile as well as further insight into the influence of the variation of the collection NA.

ACKNOWLEDGMENTS

The authors gratefully acknowledge financial support by the Deutsche Forschungsgemeinschaft (DFG) through projects CRC1415 (ID: 417590517), EN 434/41-1 (TOP-ELEC), INST 269/656-1 FUGG, and FOR5044 (ID: 426703838) as well as the Würzburg–Dresden Cluster of Excellence on "Complexity and Topology in Quantum Matter"—ct.qmat (EXC 2147; ID 39085490). Also, we would like to acknowledge the excellent support by the Light Microscopy Facility, a Core Facility of the CMCB Technology Platform at TU Dresden, where the SHG analysis was performed.

AUTHOR DECLARATIONS

Conflict of Interest

The authors have no conflicts to disclose.

Author Contributions

Peter A. Hegarty: Data curation (lead); Formal analysis (lead); Investigation (lead); Methodology (lead); Writing – original draft (equal); Writing – review & editing (equal). **Henrik Beccard:** Investigation (supporting); Methodology (supporting); Resources (equal). **Lukas M. Eng:** Funding acquisition (equal); Methodology (equal); Supervision (equal); Writing – original draft (equal); Writing – review & editing (equal).

DATA AVAILABILITY

The data that support the findings of this study are available from the corresponding authors upon reasonable request.

REFERENCES

[1]N. Kumar, S. Najmaei, Q. Cui, F. Ceballos, P. Ajayan, J. Lou, and H. Zhao, "Second harmonic microscopy of monolayer MoS_2," Phys. Rev. B **87**, 161403 (2013).
[2]S. Cherifi-Hertel, H. Bulou, R. Hertel, G. Taupier, K. Dorkenoo, C. Andreas, J. Guyonnet, I. Gaponenko, K. Gallo, and P. Paruch, "Non-Ising and chiral ferroelectric domain walls revealed by nonlinear optical microscopy," Nat. Commun. **8**, 15768 (2017).
[3]K. Spychala, P. Mackwitz, M. Rüsing, A. Widhalm, G. Berth, C. Silberhorn, and A. Zrenner, "Nonlinear focal mapping of ferroelectric domain walls in $LiNbO_3$: Analysis of the SHG microscopy contrast mechanism," J. Appl. Phys. **128**, 234102 (2020).
[4]K. Spychala, P. Mackwitz, A. Widhalm, G. Berth, and A. Zrenner, "Spatially resolved light field analysis of the second-harmonic signal of $\chi^{(2)}$-materials in the tight focusing regime," J. Appl. Phys. **127**, 023103 (2020).
[5]Z. Amber, B. Kirbus, L. Eng, and M. Rüsing, "Quantifying the coherent interaction length of second-harmonic microscopy in lithium niobate confined nanostructures," J. Appl. Phys. **130**, 133102 (2021).
[6]M. Rüsing, J. Zhao, and S. Mookherjea, "Second harmonic microscopy of poled x-cut thin film lithium niobate: Understanding the contrast mechanism," J. Appl. Phys. **126**, 114105 (2019).
[7]T. Kämpfe, P. Reichenbach, M. Schröder, A. Haußmann, L. M. Eng, T. Woike, and E. Soergel, "Optical three-dimensional profiling of charged domain walls in ferroelectrics by Cherenkov second-harmonic generation," Phys. Rev. B **89**, 035314 (2014).
[8]T. Kämpfe, P. Reichenbach, A. Haußmann, T. Woike, E. Soergel, and L. Eng, "Real-time three-dimensional profiling of ferroelectric domain walls," Appl. Phys. Lett. **107**, 152905 (2015).
[9]Y. Zhang and S. Cherifi-Hertel, "Focusing characteristics of polarized second-harmonic emission at non-Ising polar domain walls," Opt. Mater. Express **11**, 3736 (2021).
[10]S. Cherifi-Hertel, C. Voulot, U. Acevedo-Salas, Y. Zhang, O. Crégut, K. Dorkenoo, and R. Hertel, "Shedding light on non-Ising polar domain walls: Insight from second harmonic generation microscopy and polarimetry analysis," J. Appl. Phys. **129**, 081101 (2021).
[11]L. Eng and H.-J. Güntherodt, "Scanning force microscopy and near-field scanning optical microscopy of ferroelectric and ferroelastic domain walls," Ferroelectrics **236**, 35 (2000).
[12]J. Gonnissen, D. Batuk, G. Nataf, L. Jones, A. Abakumov, S. Van Aert, D. Schryvers, and E. K. Salje, "Direct observation of ferroelectric domain walls in $LiNbO_3$: Wall-meanders, kinks, and local electric charges," Adv. Funct. Mater. **26**, 7599 (2016).
[13]V. Gopalan, V. Dierolf, and D. Scrymgeour, "Defect-domain wall interactions in trigonal ferroelectrics," Ann. Rev. Mater. Res. **37**, 449 (2007).
[14]J. Kaneshiro, S. Kawado, H. Yokota, Y. Uesu, and T. Fukui, "Three-dimensional observations of polar domain structures using a confocal second-harmonic generation interference microscope," J. Appl. Phys. **104**, 054112 (2008).
[15]J. Kaneshiro, Y. Uesu, and T. Fukui, "Visibility of inverted domain structures using the second harmonic generation microscope: Comparison of interference and non-interference cases," J. Opt. Soc. Am. B **27**, 888 (2010).
[16]Y. Uesu, H. Yokota, S. Kawado, J. Kaneshiro, S. Kurimura, and N. Kato, "Three-dimensional observations of periodically poled domains in a $LiTaO_3$ quasiphase matching crystal by second harmonic generation tomography," Appl. Phys. Lett. **91**, 184902 (2007).
[17]B. Kirbus, C. Godau, L. Wehmeier, H. Beccard, E. Beyreuther, A. Haußmann, and L. Eng, "Real-time 3D imaging of nanoscale ferroelectric domain wall dynamics in lithium niobate single crystals under electric stimuli: Implications for domain-wall-based nanoelectronic devices," ACS Appl. Nano Mater. **2**, 5787 (2019).
[18]C. Godau, T. Kämpfe, A. Thiessen, L. Eng, and A. Haußmann, "Enhancing the domain wall conductivity in lithium niobate single crystals," ACS Nano **11**, 4816 (2017).
[19]M. Ayoub, P. Roedig, and K. Koynov, "Čerenkov-type second-harmonic spectroscopy in random nonlinear photonic structures," Opt. Express **21**, 8220 (2013).
[20]M. Ayoub, M. Paßlick, J. Imbrock, and C. Denz, "Simultaneous type I and type II Čerenkov-phase matched second-harmonic generation in disordered nonlinear photonic structures," Opt. Express **23**, 28369 (2015).
[21]S. Saltiel, D. Neshev, W. Krolikowski, A. Arie, O. Bang, and Y. Kivshar, "Multiorder nonlinear diffraction in frequency doubling processes," Opt. Lett. **34**, 848 (2009).
[22]A. Kaminskii, H. Nishioka, K. Ueda, W. Odajima, M. Tateno, K. Sasaki, and A. V. Butashin, "Second-harmonic generation with Cherenkov-type phase matching in a bulk nonlinear $LaBGeO_5$," J. Quantum Electron. **26**, 381 (1996).

Downloaded from http://pubs.aip.org/aip/jap/article-pdf/doi/10.1063/5.0094988/16509948/244102_1_online.pdf

© Author(s) 2022

[23]X. Deng and X. Chen, "Domain wall characterization in ferroelectrics by using localized nonlinearities," Opt. Express **18**, 15597 (2010).
[24]A. Zembrod, H. Puell, and J. Giordmaine, "Surface radiation from non-linear optical polarisation," Opt. Quantum Electr. **1**, 396 (1969).
[25]M. Ayoub, H. Futterlieb, J. Imbrock, and C. Denz, "3D imaging of ferroelectric kinetics during electrically driven switching," Adv. Mater. **29**, 1603325 (2017).
[26]M. Ayoub, J. Imbrock, and C. Denz, "Ferroelectric domain diagnostics near the phase transition by Čerenkov second-harmonic generation," Opt. Mater. Express **7**, 3448–3455 (2017).
[27]Y. Sheng, S. Saltiel, N. Voloch-Bloch, D. Neshev, W. Krolikowski, A. Arie, K. Koynov, and Y. Kivshar, "Cerenkov-type second-harmonic generation in two-dimensional nonlinear photonic structures," J. Quantum Electron. **45**, 1465 (2009).
[28]Y. Sheng, A. Best, H.-J. Butt, W. Krolikowski, A. Arie, and K. Koynov, "Three-dimensional ferroelectric domain visualization by Čerenkov-type second harmonic generation," Opt. Express **18**, 16539–16545 (2010).
[29]Y. Sheng, V. Roppo, K. Kalinowski, and W. Krolikowski, "Role of a localized modulation of $\chi^{(2)}$ in Čerenkov second-harmonic generation in nonlinear bulk medium," Opt. Lett. **37**, 3864–3866 (2012).
[30]Y. Sheng, Q. Kong, V. Roppo, K. Kalinowski, Q. Wang, C. Cojocaru, and W. Krolikowski, "Theoretical study of Čerenkov-type second-harmonic generation in periodically poled ferroelectric crystals," J. Opt. Soc. Am. B: Opt. Phys. **29**, 312–318 (2012).
[31]Y. Sheng, V. Roppo, M. Ren, K. Kalinowski, C. Cojocaru, J. Trull, Z. Li, K. Koynov, and W. Krolikowski, "Multi-directional Čerenkov second harmonic generation in two-dimensional nonlinear photonic crystal," Opt. Express **20**, 3948–3953 (2012).
[32]Y. Sheng, A. Arie, K. Koynov, and W. Krolikowski, "Cerenkov-type second hamonic generation and its application to three-dimensional nonlinear microscopy," in *PIERS 2011 Suzhou Proceedings* (The Electromagnetics Academy, 2011), p. 790.
[33]Y. Sheng, W. Wang, R. Shiloh, V. Roppo, Y. Kong, A. Arie, and W. Krolikowski, "Čerenkov third-harmonic generation in $\chi^{(2)}$ nonlinear photonic crystal," Appl. Phys. Lett. **98**, 241114 (2011).
[34]Y. Sheng, V. Roppo, Q. Kong, K. Kalinowski, Q. Wang, C. Cojocaru, J. Trull, and W. Krolikowski, "Tailoring Čerenkov second-harmonic generation in bulk nonlinear photonic crystal," Opt. Lett. **36**, 2593–2595 (2011).
[35]Y. Sheng, V. Roppo, K. Kalinowski, and W. Krolikowski, "Nonlinear Čerenkov radiation from a single ferroelectric domain wall," in *2013 Conference on Lasers & Electro-Optics Europe & International Quantum Electronics Conference CLEO EUROPE/IQEC* (IEEE, 2013), p. 1.
[36]K. Kalinowski, V. Roppo, Q. Kong, Y. Sheng, and W. Krolikowski, "Čerenkov second harmonic generation in nonlinear crystals," in *Conference on Lasers and Electro-Optics/Pacific Rim* (Optical Society of America, 2011), p. C371.
[37]K. Kalinowski, P. Roedig, Y. Sheng, M. Ayoub, J. Imbrock, C. Denz, and W. Krolikowski, "Enhanced Čerenkov second-harmonic emission in nonlinear photonic structures," Opt. Lett. **37**, 1832 (2012).
[38]H. Ren, X. Deng, Y. Zheng, and X. Chen, "Single domain wall effect on parametric processes via Cherenkov-type phase matching," J. Nonlinear Opt. Phys. Mater. **20**, 459–466 (2012).
[39]H. Ren, X. Deng, Y. Zheng, N. An, and X. Chen, "Nonlinear Cherenkov radiation in an anomalous dispersive medium," Phys. Rev. Lett. **108**, 223901 (2012).
[40]B. Liu, Y. Zheng, X. Zhao, H. Liu, and X. Chen, "Probe of symmetry reduction at domain walls by nonlinear Cherenkov measurement," Opt. Express **24**, 29459 (2016).
[41]S. Liu, K. Switkowski, X. Chen, T. Xu, W. Krolikowski, and Y. Sheng, "Broadband enhancement of Čerenkov second harmonic generation in a sunflower spiral nonlinear photonic crystal," Opt. Express **26**, 8628–8633 (2018).
[42]H. Ren, X. Deng, and X. Chen, "Coherently superposed efficient second harmonic generation by domain wall series in ferroelectrics," arXiv:1010.1593 (2010).
[43]X. Deng, H. Ren, and X. Chen, "Phase-matched second harmonic generation by enhanced nonlinearities in ferroelectric domain walls," in *CLEO: Science and Innovations* (Optical Society of America, 2011), p. JThB58.
[44]V. Shikhova, M. Nebogatikov, V. Anikin, L. Ivleva, and V. Y. Shur, "Evolution of the domain structure during polarization reversal in relaxor SBN single crystals studied by Čerenkov-type second harmonic generation microscopy," Ferroelectrics **576**, 75–84 (2021).
[45]N. An *et al.*, "The role of ferroelectric domain wall in nonlinear cerenkov frequency up-conversion in 1D nonlinear crystal," J. Nonlinear Opt. Phys. Mater. **25**, 1650008 (2016).
[46]S. Xiao, T. Kämpfe, Y. Jin, A. Haußmann, X. Lu, and L. Eng, "Dipole-tunneling model from asymmetric domain-wall conductivity in $LiNb0_3$ single crystals," Phys. Rev. Appl. **10**, 034002 (2018).
[47]G. Nataf, M. Guennou, J. Gregg, D. Meier, J. Hlinka, E. Salje, and J. Kreisel, "Domain-wall engineering and topological defects in ferroelectric and ferroelastic materials," Nat. Rev. Phys. **2**, 634–648 (2020).
[48]Y. Zhang, F. Wang, K. Geren, S. Zhu, and M. Xiao, "Second-harmonic imaging from a modulated domain structure," Opt. Lett. **35**, 178–180 (2010).
[49]A. Vyunishev, A. Aleksandrovsky, A. Zaitsev, and V. Slabko, "Čerenkov nonlinear diffraction in random nonlinear photonic crystal of strontium tetraborate," Appl. Phys. Lett. **101**, 211114 (2012).
[50]J. Imbrock, M. Ayoub, M. Paßlick, J. Hanisch, and C. Denz, "Type I and type II Čerenkov second-harmonic generation microscopy in $\chi^{(2)}$-disordered media," in *Advanced Photonics* (Optica Publishing Group, 2014), p. NTu2A.4.
[51]L. Wehmeier, T. Kämpfe, A. Haußmann, and L. M. Eng, "In situ 3D observation of the domain wall dynamics in a triglycine sulfate single crystal upon ferroelectric phase transition," Phys. Status Solidi RRL **11**, 1700267 (2017).
[52]X. Chen, P. Karpinski, V. Shvedov, W. Krolikowski, Y. Sheng, B. Wang, J. Trull, C. Cojocaru, A. Boes, and A. Mitchell, "Two-dimensional domain structures in lithium niobate via domain inversion with ultrafast light," Photonics Lett. Pol. **8**, 33–35 (2016).
[53]A. Tunyagi, M. Ulex, and K. Betzler, "Noncollinear optical frequency doubling in strontium barium niobate," Phys. Rev. Lett. **90**, 243901 (2003).
[54]J. Kaneshiro and Y. Uesu, "Domain structure analysis of $Pb(Zn_{1/3}Nb_{2/3})O_3$-9% $PbTiO_3$ single crystals using optical second harmonic generation microscopy," Phys. Rev. B **82**, 184116 (2010).
[55]Y. Uesu, S. Kurimura, and Y. Yamamoto, "Optical second harmonic images of 90° domain structure in $BaTiO_3$ and periodically inverted antiparallel domains in $LiTaO_3$," Appl. Phys. Lett. **66**, 2165 (1995).
[56]H. Yokota, S. Matsumoto, E. Salje, and Y. Uesu, "Polar nature of domain boundaries in purely ferroelastic $Pb_3(PO_4)_2$ investigated by second harmonic generation microscopy," Phys. Rev. B **100**, 024101 (2019).
[57]H. Yokota, C. R. Haines, S. Matsumoto, N. Hasegawa, M. Carpenter, Y. Heo, A. Marin, E. K. Salje, and Y. Uesu, "Domain wall generated polarity in ferroelastics: Results from resonance piezoelectric spectroscopy, piezoelectric force microscopy, and optical second harmonic generation measurements in $LaAlO_3$ with twin and tweed microstructures," Phys. Rev. B **102**, 104117 (2020).
[58]H. Yokota and Y. Uesu, "Optical second-harmonic generation microscopy as a tool for ferroelastic domain wall exploration," J. Appl. Phys. **129**, 014101 (2021).
[59]Y. Zhang, Y. Zhang, Q. Guo, X. Zhong, Y. Chu, H. Lu, G. Zhong, J. Jiang, C. Tan, M. Liao, Z. Lu, D. Zhang, J. Wang, J. Yuan, and Y. Zhou, "Characterization of domain distributions by second harmonic generation in ferroelectrics," npj Comput. Mater. **4**, 1 (2018).
[60]M. Fiebig, D. Fröhlich, T. Lottermoser, and M. Maat, "Probing of ferroelectric surface and bulk domains in $RMnO_3$(R = Y, Ho) by second harmonic generation," Phys. Rev. B **66**, 144102 (2002).
[61]X. Huang, D. Wei, Y. Wang, Y. Zhu, Y. Zhang, X. P. Hu, S. N. Zhu, and M. Xiao, "Second-harmonic interference imaging of ferroelectric domains through a scanning microscope," J. Phys. D **50**, 485105 (2017).
[62]P. Mackwitz, M. Rüsing, G. Berth, A. Widhalm, K. Müller, and A. Zrenner, "Periodic domain inversion in x-cut single-crystal lithium niobate thin film," Appl. Phys. Lett. **108**, 152902 (2016).

Downloaded from http://pubs.aip.org/aip/jap/article-pdf/doi/10.1063/5.0094988/16509948/244102_1_online.pdf

© Author(s) 2022

[63]S. Bozhevolnyi, J. Hvam, K. Pedersen, F. Laurell, H. Karlsson, T. Skettrup, and M. Belmonte, "Second-harmonic imaging of ferroelectric domain walls," Appl. Phys. Lett. **73**, 1814 (1998).
[64]S. Bozhevolnyi, K. Pedersen, T. Skettrup, X. Zhand, and M. Belmonte, "Far- and near-field second-harmonic imaging of ferroelectric domain walls," Opt. Commun. **152**, 221 (1998).
[65]M. Flörsheimer, R. Paschotta, U. Kubitscheck, C. Brillert, D. Hofmann, L. Heuer, G. Schreiber, C. Verbeek, W. Sohler, and H. Fuchs, "Second-harmonic imaging of ferroelectric domains in $LiNbO_3$ with micron resolution in lateral and axial directions," Appl. Phys. B **67**, 593 (1998).
[66]S. Denev, T. Lummen, E. Barnes, A. Kumar, and V. Gopalan, "Probing ferroelectrics using optical second harmonic generation," J. Am. Ceram. Soc. **94**, 2699 (2011).
[67]X. Gu, R. Korotkov, Y. Ding, J. Kang, and J. Khurgin, "Backward second-harmonic generation in periodically poled lithium niobate," J. Opt. Soc. Am. B **15**, 1561 (1998).
[68]Y. Gu, M. Li, A. Morozovska, Y. Wang, V. Eliseev, E. Gopalan, and L.-Q. Chen, "Flexoelectricity and ferroelectric domain wall structures: Phase-field modeling and DFT calculations," Phys. Rev. B **89**, 174111 (2014).
[69]M. Maglione, A. Theerthan, V. Rodriguez, A. Peña, C. Canalias, B. Ménaert, and B. Boulanger, "Intrinsic ionic screening of the ferroelectric polarization of KTP revealed by second-harmonic generation microscopy," Opt. Mater. Express **6**, 137 (2016).
[70]N. Mazumder, G. Deka, W. Wu, A. Gogoi, G. Zhuo, and F.-J. Kao, "Polarization resolved second harmonic microscopy," Methods **128**, 105 (2017).
[71]A. Fragemann, V. Pasiskevicius, and F. Laurell, "Second-order nonlinearities in the domain walls of periodically poled $KTiOPO_4$," Appl. Phys. Lett. **85**, 375 (2004).
[72]R. Boyd, *Nonlinear Optics* (Academic Press, London, 2020).
[73]*Properties of Lithium Niobate*, edited by K. Wong (INSPEC, The Institution of Electrical Engineers, London, 2002), Vol. 28.

Downloaded from http://pubs.aip.org/aip/jap/article-pdf/doi/10.1063/5.0094988/16509946/244102_1_online.pdf

© Author(s) 2022